Phase-Based Manganese Enhanced MRI, a New Methodology to Enhance Brain Cytoarchitectural Contrast and Study Manganese Uptake

Rajika Maddage,[1] José P. Marques,[2]* and Rolf Gruetter[1,2,3]

Purpose: As the magnetic susceptibility induced frequency shift increases linearly with magnetic field strength, the present work evaluates manganese as a phase imaging contrast agent and investigates the dose dependence of brain enhancement in comparison to T_1-weighted imaging after intravenous administration of $MnCl_2$.

Methods: Experiments were carried out on 12 Sprague-Dawley rats. $MnCl_2$ was infused intravenously with the following doses: 25, 75, 125 mg/kg (n=4). Phase, T_1-weighted images and T_1 maps were acquired before and 24h post $MnCl_2$ administration at 14.1 Tesla.

Results: Manganese enhancement was manifested in phase imaging by an increase in frequency shift differences between regions rich in calcium gated channels and other tissues, together with local increase in signal to noise ratio (from the T_1 reduction). Such contrast improvement allowed a better visualization of brain cytoarchitecture. The measured T_1 decrease observed across different manganese doses and in different brain regions were consistent with the increase in the contrast to noise ratio (CNR) measured by both T_1-weighted and phase imaging, with the strongest variations being observed in the dentate gyrus and olfactory bulb.

Conclusion: Overall from its high sensitivity to manganese combined with excellent CNR, phase imaging is a promising alternative imaging protocol to assess manganese enhanced MRI at ultra high field. **Magn Reson Med 72:1246–1256, 2014. © 2013 Wiley Periodicals, Inc.**

Key words: phase imaging; manganese enhanced MRI; MR phase contrast agent; high field MRI

INTRODUCTION

Contrast agents have been regularly used to improve the contrast between and within soft tissues and overcome the limits of the available contrast originating from differences in relaxation times (T_1/T_2), spin mobility (diffusion, perfusion), and spin density. By affecting the longitudinal and the transverse relaxation rate of surrounding water protons, paramagnetic and superparamagnetic contrast agents enhance the contrast to noise ratio (CNR) by either increasing or reducing the signal in targeted regions.

Manganese (Mn^{2+}) has proven to be a very interesting MR contrast agent. Being an analog to $Ca2^{+}$ and paramagnetic (due to the five unpaired electrons on the 3d electronic orbital), Mn^{2+} can enter voltage gated calcium channels and enhance the signal in T_1-weighted images in regions of Mn^{2+} accumulation due to local T_1 shortening. Studies using Mn^{2+} as a contrast agent have been limited to animal models because of its high cellular toxicity, causing heart and hepatic failure (1,2), and, in the case of chronic Mn^{2+} exposure, leading to a form of Parkinsonism (3). In rodents, various in vivo brain studies have been performed to map neuronal connections (4), functional activity (5), and enhance the brain cytoarchitecture (6,7), demonstrating to be an useful MRI marker of neuronal activity and calcium influx in tissues. As Mn^{2+} is not able to cross the blood brain barrier (BBB) three main approaches have been used to deliver Mn^{2+} to the targeted brain regions: infusion of Mn^{2+} followed by BBB disruption (8); local injection (4); systemic administration, with the enhancement being first observed in choroid plexus, cerebrospinal fluid, and only latter in tissues (9). The least invasive method, systemic administration, has enabled to depict several structures rich or with active voltage gated calcium channels such as layers in the hippocampus, cortex, and olfactory bulb (6,7,10).

Over the recent years, phase imaging has gained a significant interest (11,12) thanks to the increase of the magnetic fields available on clinical MR scanners. At fields above 3 Tesla, it was shown that the contrast to noise ratio (CNR) observed in phase images between gray and white matter was superior to that of conventional magnitude images, yielding additional anatomical information in the brain including the observation of subcortical contrast (11,12). In rodent studies, phase imaging at high magnetic field with an in-plane resolution of 33 μm was found to give anatomical details with clear depiction of cytoarchictectural features such as hippocampal fields, cortical and cerebellar layers, structures typically not easily discernible in T_1, T_2, or T_2* magnitude images (13).

The observed contrast in phase imaging is due to magnetic susceptibility induced frequency shifts which increase linearly with the magnetic field strength. Even though its origin is still not clear, many mechanisms have been proposed (11,14,15) with tissue bulk magnetic susceptibility playing a major role in modulating the phase shifts observed across the brain. The origin of such bulk susceptibility has been found to have

[1]Laboratory for Functional and Metabolic Imaging, École Polytechnique Fédérale de Lausanne, Lausanne, Switzerland.

[2]Department of Radiology, Université de Lausanne, Lausanne, Switzerland.

[3]Department of Radiology, Université de Geneve, Geneve, Switzerland.

*Correspondence to: José P. Marques, Ph.D., EPFL SB CIBM-AIT, CH F0 582 (Bâtiment CH), Station 6, CH-1015 Lausanne, Switzerland. E-mail: jose.marques@epfl.ch

Received 13 May 2013; revised 16 October 2013; accepted 16 October 2013

DOI 10.1002/mrm.25037

Published online 20 November 2013 in Wiley Online Library (wileyonlinelibrary.com).

different origins in different brain regions. In humans, the contrast observed in deep gray matter nuclei and in intracortical contrast has been attributed to local iron concentration (16,17), while in rodents, the susceptibility difference responsible for gray and white matter contrast has been demonstrated to have myelin origin (18–20).

To the best of our knowledge, manganese enhanced MRI (MEMRI) has only been assessed using T_1 contrast. The increasingly strong magnetic fields available potentiate stronger Mn^{2+} magnetic susceptibility effects, making phase imaging a natural candidate to profit from Mn^{2+} uptake in tissues. Mn^{2+} should induce a phase shift observable with phase imaging and, combined with its high sensitivity to endogenous magnetic susceptibility distribution and high CNR, could be exploited to further enhance neural architecture in animal models.

The present work was designed to investigate the above hypothesis by assessing Mn^{2+} potential input on phase imaging at 14.1T and to determine the level of phase contrast enhancement obtained following systemic administration in comparison to the standard imaging protocol used in MEMRI, namely T_1-weighted imaging. The phase shift and the contrast enhancement as a function of the Mn^{2+} dose were also investigated to assess its linearity and sensitivity in comparison to T_1-weighted imaging. Finally, the potential of quantification of Mn^{2+} uptake based on phase imaging is addressed.

METHODS

Animal Preparation

Experiments were carried out in 12 male Sprague-Dawley rats (weighting 200–300 g). All animal experiments were conducted according to federal and local ethical guidelines and the protocols were approved by the local regulatory body.

The Mn^{2+} administration protocol consisted of a tail vein infusion at a rate of 1.0 mL/h of an isotonic $MnCl_2$ (Sigma-Aldrich, St Louis, MO) solution prepared with a concentration of 120 mM. During $MnCl_2$ infusion, all rats were anesthetized under 2% isoflurane and their body temperature was maintained at 38 ± 0.5°C by means of a heating pad. Four different doses of $MnCl_2$ were used: 25 (4 animals), 75 (4 animals), 125 (4 animals), and 175 mg/kg. The dose of 175 mg/kg was discarded due to a high mortality rate observed (90%). After infusion, rats were returned to their cages with free access to food and water and held under a 12 h/12 h light/dark regimen.

MRI was performed prior and 24h post $MnCl_2$ infusion. During the MR image acquisition, the rats were kept under anesthesia (1.5–2% isoflurane delivered through a face mask) and were fixed using a custom made stereotaxic holder. Respiration rate was monitored using a pressure pillow placed under the rat's abdomen (respiration rate of 60 ± 3 breaths per minute). Body temperature was monitored using a rectal temperature probe and maintained at 38 ± 0.5°C by a heated water bath.

Phantom Study: $MnCl_2$ Relaxometry at 14.1T

A phantom containing seven cylindrical tubes with different Mn^{2+} concentration (from 0 μM to 200 μM dissolved in distilled water) was produced. From the T_1 ($1/R_1$) and frequency shift maps measured across the Mn^{2+} concentrations, it was possible to compute the relaxivity parameters r_1 and magnetic susceptibility $\chi([Mn^{2+}])$. (Details of the imaging and processing protocols will be given in the MRI and Phantom Data sections respectively).

MRI

All scans were performed on a 14.1T/26 cm horizontal bore magnet (Varian/Magnex Scientific). The $MnCl_2$ relaxometry protocol (performed on the phantom described on the previous paragraph) was acquired using a high pass birdcage coil with an inner diameter of 46 mm and length of 30 mm. In vivo rat brain images were acquired using a home built quadrature surface coil as radiofrequency (RF) transceiver with two geometrically decoupled 21 mm loops resonating at 600 MHz. To take full advantage of the high signal to noise ratio (SNR), the surface coil was carefully and systematically positioned over the brain regions under investigation, regions known to be rich/or with active voltage gated calcium channels that are susceptible to Mn^{2+} uptake (6,7): olfactory bulb (OB) including the olfactory nerve layer (ONL), glomerular layer (GL) and mitral cell layer (ML); the hippocampus (HC) including the CA formation of the hippocampus and the dentate gyrus. To take advantage of using thick slices (compared with the in-plane resolution) and to further improve the SNR without significantly increasing partial volume effects, both the slices covering the hippocampus and the olfactory bulb were positioned coronally.

Magnetic field homogeneity was adjusted using FASTMAP (21) in a large volume located in the different regions. Water spectra linewidth of 21–26 Hz were obtained over a typical voxel size of $7 \times 10 \times 6$ mm^3 in cortex/hippocampus regions and $2 \times 2 \times 4$ mm^3 in the OB. The complete acquisition protocol described in the following paragraph was applied before and 24h post Mn^{2+} systemic administration.

T_1 Mapping

T_1 mapping was performed using a multi-slice multishot inversion-recovery Look-Locker Segmented Echo Planar Imaging sequence (22,23). A slice-selective 180° adiabatic pulse (hyperbolic secant, hs8) was used to invert the magnetization followed by low flip angle slice-selective pulses (FA = 20°) that sampled the inversion recovery curve in 20 points with inversion times from 50 ms to 4050 ms (with an inter-excitation delay of 200 ms). The repetition time (TR) was set to 24.5 s, sufficient for the full recovery of the longitudinal magnetization allowing 6 slices to be acquired per TR while the interexcitation delay was chosen to guarantee the accuracy of T_1 values down to 400 ms (22,23). The echo time (TE) of the EPI readout was kept short (TE = 5.7 ms) to avoid through slice signal dephasing. K-space was

acquired in a segmented manner (16 shots) to reduce geometrical distortions due to magnetic susceptibility differences (tissue/air). Other imaging parameters: field of view (FOV) = 22*22 mm^2, resolution = 172*172*800 μm^3, number of slices = 6 and total acquisition time = 14 min. For Nyquist ghost correction, a readout polarity reversal scheme was used (24).

T_1-Weighted and Phase Images

T_1-weighted and phase images were acquired using a gradient echo multi-slice sequence (GEMS) with respiration gating to reduce respiration induced artifacts which suggested that all images were acquired with a TR~1s. The small and slow variations in respiration rate could only generate a maximum signal variation (due to TR fluctuations) of ±4%, which was considered too small to require any extra corrections.

For phase images, the flip angle was optimized to maximize the signal intensity in the specific regions of interest. The echo time (16 ms) was chosen to approximately match the gray matter T_2* and, hence, optimize phase contrast (13). The acquisition bandwidth was chosen to maximize signal without introducing effective resolution reduction due to T_2* decay during the readout (tacq = 15.9 ms).

For T_1-weighted images, echo time was reduced (5 ms) and acquisition bandwidth was increased to emphasize the T_1 contrast while maintaining sufficient SNR. The flip angle was chosen to be close to 90° to enhance the T_1 contrast in the regions where contrast enhancement was expected, while avoiding undesirable inversions in the regions closest to the coil.

Summary of acquisition parameters: TR~1s (respiration gating), TE = 5 ms(T_1-weighted)/16 ms(Phase), FA = 90°(T_1-weighted)/50°(Phase), number of slices = 20 with 0.2-mm gap to avoid cross excitation between slices. The image resolution in the different regions was 66*66*400 μm^3 (Cortex /hippocampus), 58*58*400 μm^3 (OB) with a total acquisition time of 8 min (Cortex/hippocampus, OB).

Frequency Shift Maps

To establish the magnetic susceptibility of Mn^{2+} in the phantom, frequency shift maps were acquired using a multi-gradient echo sequence. Fifteen gradient echo images (4.5 to 60.5 ms) were obtained with the following parameters: TR = 900 ms, FA = 40°, FOV = 30*30 mm^2, resolution = 234*234*800 μm^3.

Data Processing

T_1 maps were calculated pixel by pixed using a Nelder-Mead fitting algorithm (25). Due to the coil setup (surface coil) a three-parameter fit (T_1, M_0 and flip angle α) was done to take into account the transmit field inhomogeneity. Steady state signal was considered in the algorithm to remove any bias from possible magnetization not fully recovered at the end of the TR. Frequency maps were established from a linear fit to the phase change over the 15 echoes. Phase images were unwrapped (26) and the background field contributions originating from imperfect shimming, air tissue interfaces were filtered using the SHARP algorithm (17). This methodology does not remove entirely phase variations related to the transmitting and receiving B_1 field which can be removed by applying a high pass filter with a wide Gaussian width.

Phantom Data

Regions of interest (ROIs) were placed within each $MnCl_2$ tube. The relaxation rate R_1 and frequency values were measured from the respective T_1 and frequency maps for each ROI . The different values were then plotted as a function of [Mn^{2+}] and a linear regression was performed to find the longitudinal relaxivity, r_1, of Mn^{2+}

$$R_1([Mn^{2+}]) = R_1(0) + r_1 \cdot [Mn^{2+}]. \quad [1]$$

For the frequency map, the outside compartment ([Mn^{2+}]=0) was used as a reference. A frequency shift per millimolar, δf_{pmM}, was calculated

$$\Delta f([Mn^{2+}]) = \delta f_{pmM} \cdot [Mn^{2+}]. \quad [2]$$

Subsequently, the magnetic susceptibility per millimolar was calculated using the following expression $\delta f_{pmM} = -1/3*\gamma B_0 \chi_{pmM}$ (27), where γ is the gyromagnetic constant ratio, which represents the relationship between the frequency shift difference and the susceptibility difference for an infinite cylinder aligned along the main magnetic field.

In Vivo Data

The changes in T_1 due to Mn^{2+} as a function of the different doses were calculated by selecting ROIs in the cortex, hippocampus, corpus callosum (within the same slice) and in different fields of the OB (Fig. 4). Although manganese can be transported by means of the axons (28), its enrichment in white matter is limited as it mainly accumulates in synaptic regions of gray matter (29). To measure the contrast enhancement throughout the Mn^{2+} doses, the CNR was calculated as the signal difference between the tissue of interest and a region devoid of Mn^{2+} enhancement (WM) divided by the standard deviation of the noise (σ). The T_1-weighted contrast of the cortex and dentate gyrus of the hippocampus were established in respect to the corpus callosum whereas the contrast of the OB was established by subtracting the signal from the anterior commissure, intrabulbar part (aci) (Fig. 4).

Likewise, phase enrichment ($\Delta f_{GM\text{-}WM}$) and phase CNR were established considering ROI's in the same slice and the latter was calculated using the following equation:

$$CNR_{phase} = Signal_{av}.2\pi.TE.|f_{GM}\text{-}f_{WM}|/\sigma. \quad [3]$$

With $Signal_{av}$ =($Signal_{GM}$ + $Signal_{WM}$)/2, TE the echo time used, f_{GM} and f_{WM} the frequency shift of gray matter and white matter, respectively, and σ the standard deviation of the background noise measured outside the brain within artifact free regions (11).

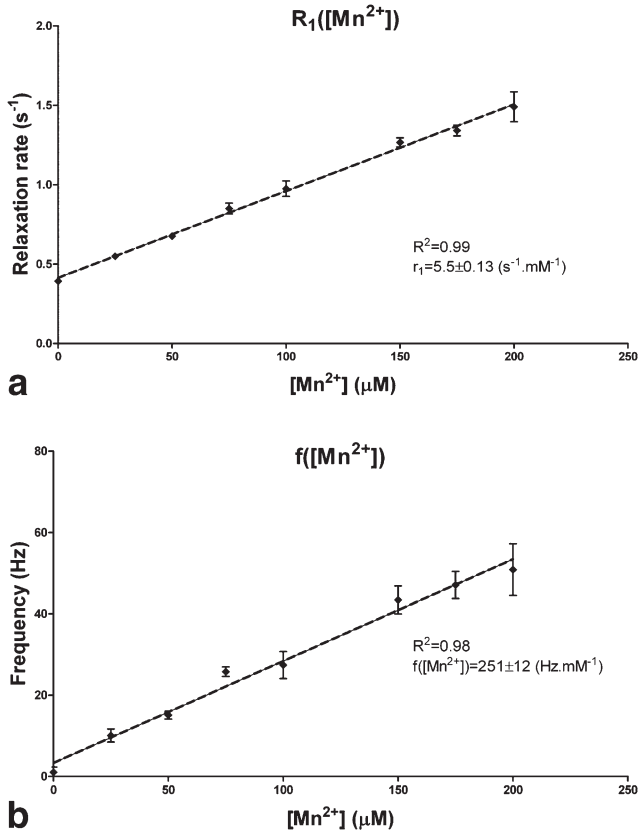

FIG. 1. In vitro relaxivity measurements of Mn^{2+} at 14.1T. **a:** Longitudinal relaxation rate R_1. **b:** Frequency shift plotted as function of [Mn^{2+}]. Error bars represent standard deviations over the regions of interest. Dashed line represents the linear regression fit to the data points.

RESULTS

Relaxivity r_1 and δf_{pmM} of Mn^{2+} at 14.1T

To determine the relaxivity parameters of Mn^{2+} at 14.1T, the relaxation rates, R_1, and frequency shifts, Δf, were measured using a phantom containing seven cylindrical tubes with Mn^{2+} concentrations ranging from 0 to 200 μM, (Fig. 1). Both quantities showed the expected linear relationship with Mn^{2+} concentration ($R^2 > 0.98$). The measured longitudinal relaxivity, r_1, was established at 5.5 ± 0.1 $s^{-1}.mM^{-1}$ (Fig. 1a). The frequency shift as a function of Mn^{2+} δf_{pmM} was measured at 251 ± 12 $Hz.mM^{-1}$ (Fig. 1b) resulting in a susceptibility of Mn^{2+} of −1.25 ± 0.06 $ppm.mM^{-1}$.The apparent transverse relaxivity r_2* was also established at 234 ± 8 $s^{-1}.mM^{-1}$ (data not shown).

Induced Phase and T_1 Changes 24h Post Systemic Mn^{2+} Administration

T_1-weighted imaging

To qualitatively determine the effect of systemic Mn^{2+} administration on T_1 contrast, T_1-weighted images of the olfactory bulb, cortex, and hippocampus acquired before and 24h after a 125 mg/kg systemic Mn^{2+} administration were compared (Fig. 2).

Before Mn^{2+} administration, tissue structures in the OB, cortex, and hippocampus regions were poorly discernible despite the high in-plane resolution of 58μm (Fig. 2).

Twenty-four hours after Mn^{2+} systemic administration, an overall increase in SNR was observed in all regions (OB: +31%; cortex +38%; hippocampus: +66%) followed by a significant increase in tissue contrast in manganese-enhanced structures. In the OB, several anatomic features were enhanced and well depicted such as the external plexiform (EPL), internal plexiform (IPL), the mitral cell layer (ML), granular cell layer (GrL), and olfactory nerve layer (ONL. Subregional anatomic structures of the hippocampus were also well visualized with clear depiction of CA1, CA2, CA3, DG of the hippocampus (black arrows Fig. 2).

Phase imaging

To qualitatively determine the effect of Mn^{2+} on phase contrast, phase images acquired before and 24h after a 125 mg/kg Mn^{2+} administration, in the same slices/regions of interest as the T_1-weighted images, were compared (Fig. 3).

Before Mn^{2+} administration, the high contrast to noise ratio (CNR) given by the phase image already enabled to depict several structures of the olfactory bulb such as the external plexiform (EPL) and internal plexiform (IPL), granular cell layer (GrL), and olfactory nerve layer (ONL) (Fig. 3). Twenty-four hours following Mn^{2+} administration, Mn^{2+} accumulation resulted in an increase of CNR in all structures rich or with active voltage gated calcium channels, further enhancing the cytoarchitectural features (black arrows Fig. 3) which were already depicted beforehand with a clear emphasis of the mitral cell layer (ML) and the glomerular layer (GL).

Likewise, in the cortex-hippocampus region and before Mn^{2+} administration, phase imaging yielded substantial anatomical contrast allowing the identification of hippocampus structures, gray matter cortical layer (Fig. 3) and white matter structures such as the corpus callosum, the internal capsule, and the fornix (as expected from previous studies). A phase shift and CNR increase mainly in the dentate gyrus, CA of the hippocampus and cortical layer (black arrows Fig. 3) was likewise observed twenty four hours following Mn^{2+} administration further enhancing the cytoarchitectural features which were already depicted beforehand.

Dose Dependence of T_1 and Phase Contrast following Mn^{2+} Systemic Administration

To define the effect of the dose of Mn^{2+} administration on both T_1 and phase images, the Mn^{2+} dose was varied from 0, 25, 75, and 125 mg/kg. Figure 4 shows the corresponding T_1 map, phase and T_1-weighted images acquired in the cortex-hippocampus and olfactory bulb regions with Mn^{2+} doses ranging from 0 to 125 mg/kg.

At the lowest dose for both phase and T_1-weighted images, enhancement of the CA1, CA2, CA3, and DG of the hippocampus (Fig. 4a) and external, internal plexiform, mitral cell, olfactory nerve, and granular cell layers (Fig. 4b) were already visible. In comparison to the cortex-hippocampus region, the contrast enhancement in the olfactory bulb was more pronounced for both imaging methods.

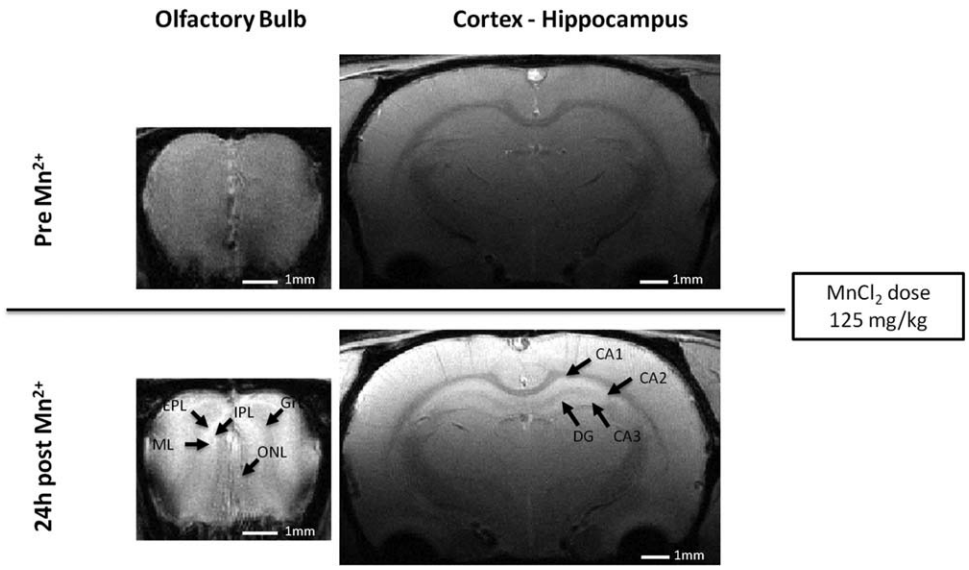

FIG. 2. Axial T_1-weighted images of the Olfactory Bulb, Cortex and Hippocampus before and 24h post $MnCl_2$ i.v. systemic administration (dose of 125 mg/kg). Pronounced signal and contrast enhancement of the brain cytoarchitecture with clear depiction of the CA1, CA3, DG of the hippocampus and olfactory bulb layers (black arrows). EPL: external plexiform; IPL: internal plexiform; ML: mitral cell layer; ONL: olfactory bulb nerve layer; GrL: granular cell layer; DG: dentate gyrus.

Such enhancement progressed with the increasing doses of Mn^{2+}, offering a better delineation of the cytoarchitectural features cited above in both imaging methods. These observations were supported by the observed T_1 decrease in the corresponding T_1 maps. Quantification of the R_1 increase is shown in Figure 5a as the evolution of the relaxation rate ΔR_1 in regions of Mn^{2+} enhancement and in white matter as a function of the Mn^{2+} dose. (Preinfused R1: Cortex: $0.42s^{-1} \pm 0.01$; Dentate Gyrus: $0.46s^{-1} \pm 0.01$; Olfactory Bulb: $0.46s^{-1} \pm 0.03$; Corpus callosum: $0.51s^{-1} \pm 0.02$). ΔR_1 was calculated for a specific ROI as the difference in relaxation rate between a given Mn^{2+} dose and preinfusion control. From 0 mg/kg to 125 mg/kg, ΔR_1s in all regions increased, with the dentate gyrus showing a greatest increase indicating a higher Mn^{2+} uptake followed by the olfactory bulb and cortex. ΔR_1 of the corpus callosum showed minimal increase throughout the Mn^{2+} doses ($+0.02s^{-1} \pm 0.03$ from 0 to 125 mg/kg).

Figure 5b shows the evolution of the frequency shift difference Δf as a function of Mn^{2+} dose measured in the same ROIs as in Figure 5a. Δf was calculated in the same manner as ΔR_1. However, as the frequency is not absolute (due to background field removal), Δf was

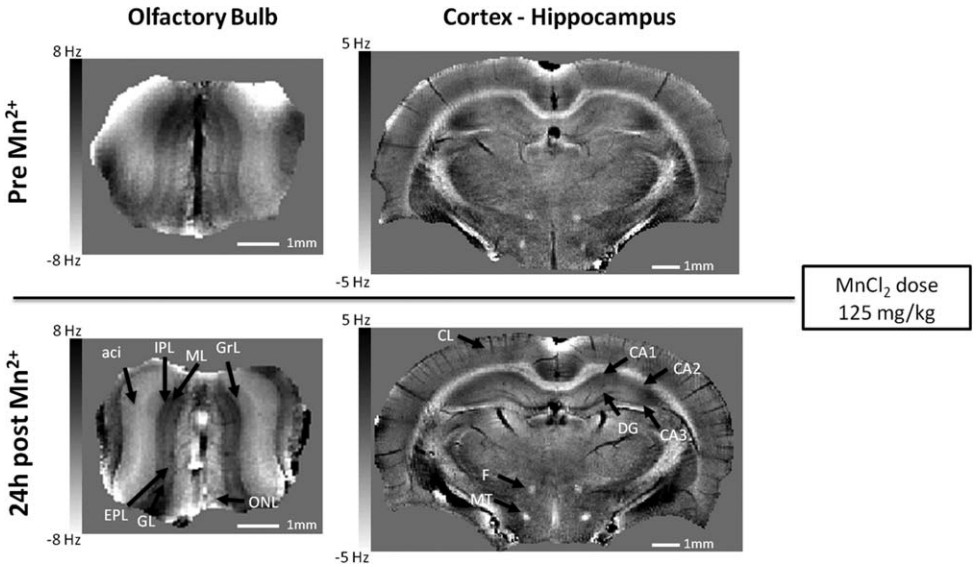

FIG. 3. Axial gradient echo phases images of the olfactory bulb, cortex and hippocampus before and 24h post $MnCl_2$ i.v. systemic administration (dose of 125 mg/kg). Pre Mn^{2+} phase images with in plane resolution of 58 μm/OB and 66 μm/Cortex-hippocampus region acquired in 8 min show good CNR between GM and WM structures enabling to already depict several tissue structures only seen in T_1-weighted images following Mn^{2+} systemic administration. Twenty-four hours post Mn^{2+} infusion, Mn^{2+} accumulation in regions rich or with active calcium channels resulted in a positive phase shift from the induced magnetic susceptibility and an increase in phase CNR. EPL: external plexiform; IPL: internal plexiform; ML: mitral cell layer; ONL: olfactory bulb nerve layer; GrL: granular cell layer; DG: dentate gyrus; F: fornix; MT: mammillothalamic tract.

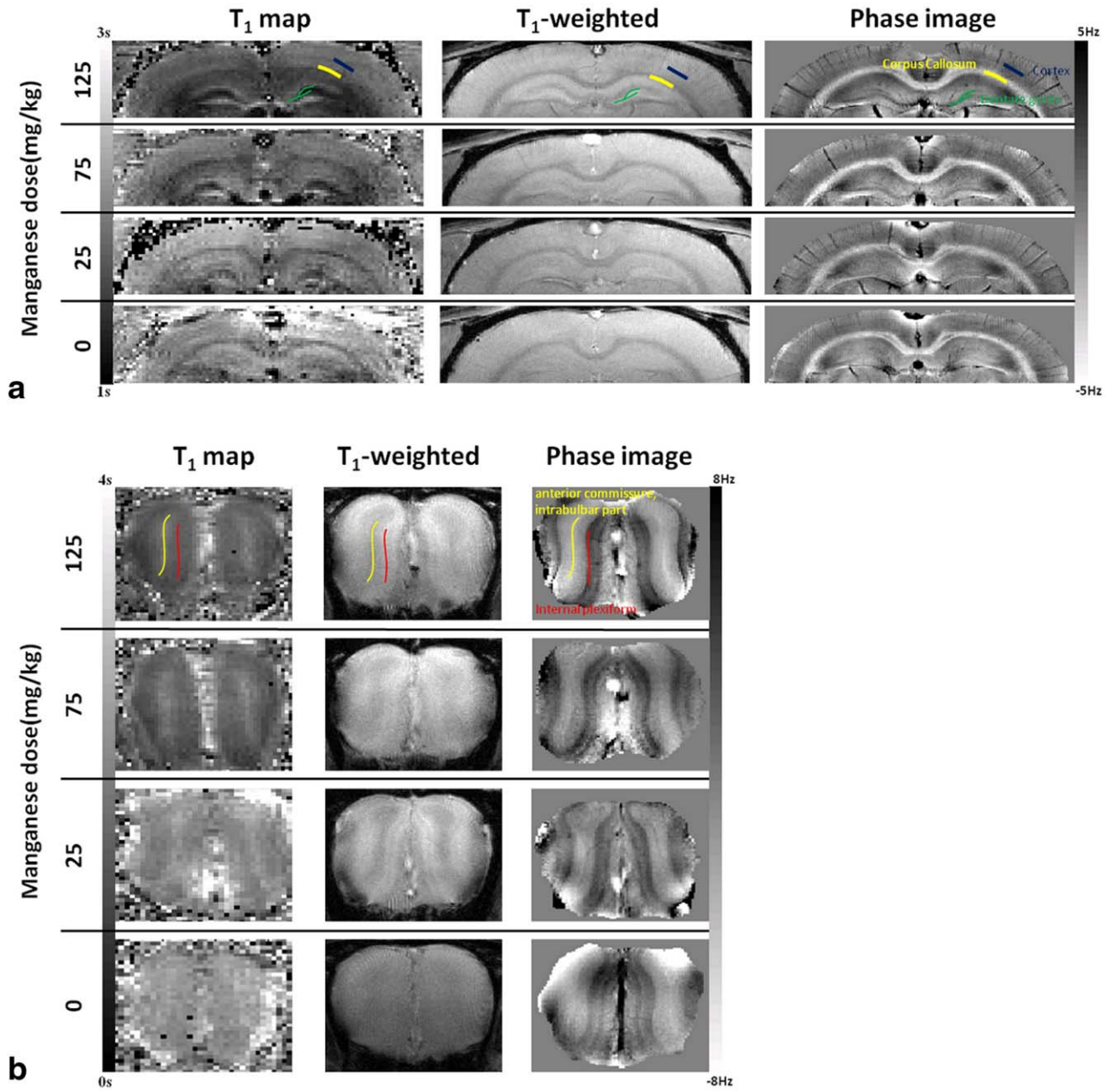

FIG. 4. Dose dependence of MEMRI contrast in cortex-hippocampus region (**a**) and OB (**b**) observed in corresponding T_1 map, T_1-weighted and phase images taken from the same animal. From the lowest dose of 25 mg/kg, brain cytoarchitecture is enhanced in both T_1-weighted and phase images with improved CNR and SNR which increased with respect to Mn^{2+} dose offering clear delineation of several subregional structures in the hippocampus and olfactory bulb. Signal intensity of T_1-weighted images has been normalized by the standard deviation of the background noise calculated from an artifact free region. Regions of interest drawn for quantification analysis are shown in the 125 mg/kg images for (a) and (b). [Color figure can be viewed in the online issue, which is available at wileyonlinelibrary.com.]

established by subtracting respectively the frequency value of the white matter in both Mn^{2+} and preinfusion control data (corpus callosum for the cortex and dentate gyrus; anterior commissure intrabulbar part for the olfactory bulb—yellow regions in Figs. 3 and 4). Again, a monotonic increase of the frequency difference as a function of Mn^{2+} uptake is observed. The smallest increase of Δf was again observed in the cortex. However, in opposition to ΔR_1, the olfactory bulb showed the greatest Δf increase.

T_1-Weighted and Phase CNR Comparison

To compare the sensitivity of phase imaging and T_1-weighted images at 14.1T, the dose dependence of the CNR was compared for both imaging methods and in the same regions of interest as described in the "Data Processing" paragraph. CNR for both imaging methods was established by subtracting the signal of neighboring white matter for each region and for each given Mn^{2+} dose. Figure 6 and Table 1 show that with increasing

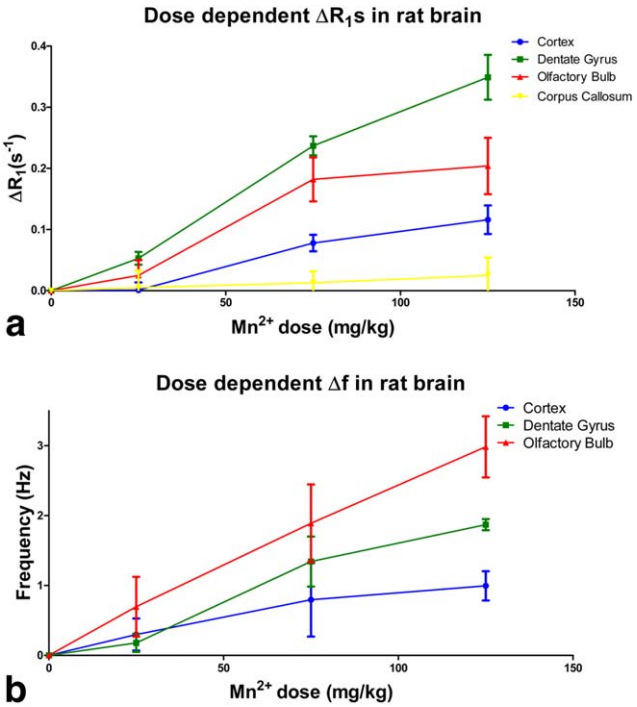

FIG. 5. ΔR_1 (**a**) and Δf (**b**) evolution, function of manganese dose across different brain regions. For a specific region of interest (ROI), ΔR_1 and Δf were established as follows: $\Delta R_1(Mn^{2+}{}_{dose}) = R_1(Mn^{2+}{}_{dose}) - R_1(0)$ with $R_1(0)$, preinfusion control R_1 value for corresponding brain region. Likewise, $\Delta f(Mn^{2+}{}_{dose}) = (f(Mn^{2+}{}_{dose}) - f_{WM}(Mn^{2+}{}_{dose})) - (f(0) - f_{WM}(0))$. Δf in the dentate gyrus and cortex was measured by subtracting the WM frequency of the corpus callosum in both Mn^{2+} and preinfusion control data. Δf of the olfactory bulb was measured by subtracting the WM frequency of the anterior commissure, intrabulbar part. From 0 mg/kg to 125 mg/kg, the dentate gyrus showed the highest increase indicating a higher Mn^{2+} uptake followed by the olfactory bulb and cortex. Likewise, a monotonic increase of the frequency difference as a function of Mn^{2+} uptake was observed in all regions. The smallest increase of Δf was again observed in the cortex. However, in opposition to ΔR_1, the olfactory bulb showed the highest Δf increase. [Color figure can be viewed in the online issue, which is available at wileyonlinelibrary.com.]

Mn^{2+} dose, both phase and T_1-weighted CNR increased progressively in all regions of interest. Globally, phase contrast outperformed our T_1-weighted imaging protocol showing always greater contrast. Also the CNR increase was greater in 7 of the 9 regions studied for the phase contrast when compared with the T_1-weighted contrast. In terms of relative increase of the CNR (relative to the initial contrast, see values inside the brackets on Table 1) between the control region and the regions with active Mn^{2+} uptake, T_1-weighted images showed superior fractional CNR increase in 6 of the 9 regions studied.

DISCUSSION

The study reports for the first time the longitudinal relaxivity parameters (r_1) and the magnetic susceptibility χ_{pmM} of Mn^{2+} at 14.1T. Magnetic susceptibility values demonstrate that Mn^{2+} enhancement could be explored in phase imaging (Fig. 1). The relaxivity of Mn^{2+} established from the measurements of R_1 to varying Mn^{2+} concentrations was in good agreement with r_1 reported at 1.5T (29) and at 11.7T (30).

These in vitro observations were confirmed in vivo with enhancement of regions rich in voltage gated calcium channels in both phase and T_1-weighted images 24h following Mn^{2+} administration (as seen Figs. 3 and 2, respectively). The results from the T_1-weighted images are consistent with previous MEMRI studies (6,7,10). Mn^{2+} enhancement was manifested in T_1-weighted imaging by a signal increase due to the reduction in T_1. In phase imaging, Mn^{2+} uptake not only resulted in increased frequency shift differences (penultimate term of Eq. [3]) but also in increased SNR due to the reduction in T_1 (first term of Eq. [3]). Mn^{2+} uptake also introduces a signal attenuation due to T_2^* decay which could hamper, at high magnetic field, the assessment of MEMRI contrast by phase imaging for high Mn^{2+} concentrations and long echo times. However, for the typically Mn^{2+} concentrations found in vivo, it should be noted that this is not a concern as the phase CNR continues to increase (see Appendix 1). The gain in phase contrast associated with T_1 reduction and increased frequency shift make phase imaging, and potentially susceptibility mapping, a promising tool in the field of MEMRI.

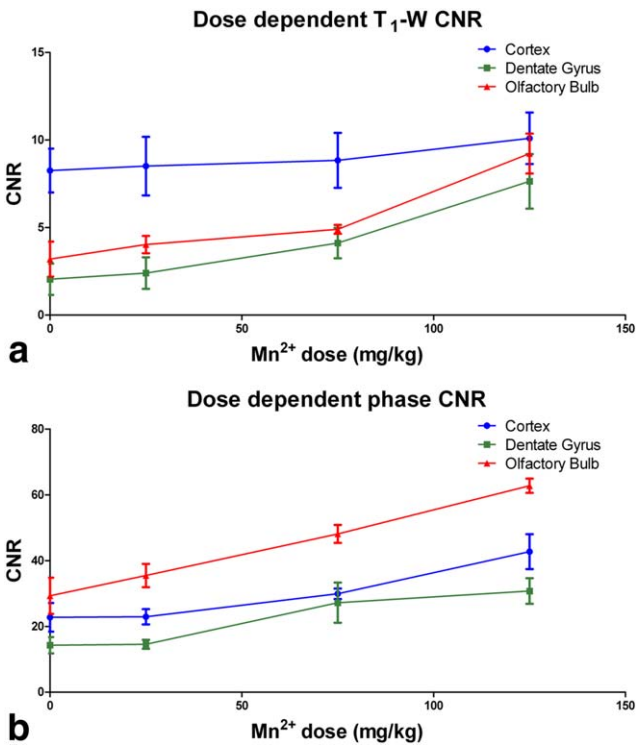

FIG. 6. Plots of the contrast to noise ratio of T_1-weighted (**a**) and phase imaging (**b**) as a function of the manganese dose for different brain regions (cortex, dentate gyrus, and olfactory bulb). At control level and for all regions, phase CNR was significantly higher than T_1-weighted CNR. From 0 to 125 mg/kg, both phase and T_1-weighted CNR increased progressively in all regions of interest. The cortex exhibited the slowest CNR increase in both imaging methods while the dentate gyrus and olfactory bulb showed the highest. [Color figure can be viewed in the online issue, which is available at wileyonlinelibrary.com.]

Table 1
Mn^{2+} Dose Dependence T_1-Weighted and Phase CNR Values in Different Brain Regions in Respect to Neighboring White Matter Regions[a]

Mn^{2+} dose (mg/kg)	Cortex		Dentate gyrus		Olfactory bulb	
	T1W CNR	Phase CNR	T1W CNR	Phase CNR	T1W CNR	Phase CNR
0	8.3 ± 1.4	22.8 ± 5.0	2.0 ± 1.0	14.3 ± 2.9	3.2 ± 1.2	29.3 ± 6.3
25	8.5 ± 1.9 (2.4%)	22.9 ± 2.7 (0.4%)	2.4 ± 1.0 (20.0%)	14.5 ± 1.6 (1.4%)	4.0 ± 0.6 (25.0%)	35.5 ± 4.1 (21.2%)
75	8.8 ± 1.8 (6.0%)	29.9 ± 1.8 (31.1%)	4.1 ± 1.0 (105.0%)	27.2 ± 7.1 (90.2%)	4.9 ± 0.3 (53.0%)	48.1 ± 3.1 (64.2%)
125	10.1 ± 1.7 (21.7%)	39.4 ± 0.8 (72.8%)	7.6 ± 1.8 (280.0%)	41.2 ± 4.8 (188.1%)	9.2 ± 1.3 (187.5%)	62.7 ± 2.6 (114%)

[a]In between brackets, the percentage increase of contrast in respect to the contrast observed in absence of Mn^{2+} administration is shown.

Before Mn^{2+} infusion, phase imaging, thanks to its high CNR between and within gray and white matter, allowed the depiction of structures which are only discernible after Mn^{2+} infusion in T_1-weighted imaging (see Figs. 2 and 3). Furthermore, other tissue structures such as white matter fiber tracts (fornix and mamillothalamic tract) not detectable on T_1-weighted images both before and after Mn^{2+} enhancement were clearly discernible in phase images. Overall, by further increasing phase CNR which was, before Mn^{2+} infusion, higher than in the T_1-weighted imaging, Mn^{2+} infusion enabled to further explore the brain structure and give additional information in comparison to the used T_1-weighted imaging protocol. As such, Mn^{2+} can be considered as a MR phase contrast agent used to enhance neuro-architectonic contrast.

Twenty-four hours following Mn^{2+} administration, veinous structures were more pronounced, indicating an increase of susceptibility present in the veins that could be either due to an increase in the deoxyhemoglobin or manganese concentration. Independently of the origin of such vessel susceptibility changes, it has been shown that point-like susceptibility inclusions inside the vasculature contribute only to a very small extent to the phase contrast between gray and white matter (13,31). Its contribution can be ruled out making the observed increase of contrast in tissue to be associated to the Mn^{2+} uptake in those regions.

The sensitivity of phase-based Mn^{2+} enhancement at 14.1T was also studied at different Mn^{2+} doses and compared with T_1-weighted imaging in different brain ROIs. Qualitatively in Figures 3 and 4, contrast in regions rich or with active voltage gated calcium channels such as the dentate gyrus, cortex, and olfactory bulb continued to increase with the increasing Mn^{2+} doses for both imaging methods offering a better delineation of the cytoarchitectural features. Quantification of R_1 changes from the T_1 maps, in the selected brain regions cited above, indicated a heterogeneous R_1 increase/Mn^{2+} uptake throughout the Mn^{2+} doses with the cortex exhibiting the smallest increase and the olfactory bulb and dentate gyrus the strongest increase (Fig. 5a and Table 1). These results are in agreement with a previous study made by Lee et al (9). The very low, but constant, R_1 increase observed in the corpus callosum ($+0.02s^{-1} \pm 0.03$ from 0 to 125 mg/kg) is a confirmation of the very weak presence of voltage gated calcium channels in white matter (32). Mn^{2+} distribution by means of the cerebrospinal fluid and paravascular spaces following systemic administration are the main pathways of Mn^{2+} enhancement in the rat brain (9). Nonspecific diffusion of Mn^{2+} ions might have an influence on the minimal R_1 increase seen in the corpus throughout the Mn^{2+} doses. Alternatively, it could also be a consequence of the relatively low resolution of the T_1 maps and the point spread function due to the EPI readout, making the increase in R_1 observed in the WM simply a partial volume effect. Nevertheless, the corpus callosum R_1 increase was very weak (when compared with the remaining regions) and could be considered non significant for the CNR study. From 0 to 125 mg/kg, both Δf and ΔR_1 increased monotonically in all regions despite correlation between ΔR_1 and Δf being different in the selected brain regions (8.8 in cortex, 5.4 in the DG and 13.1 in the OB). Nonetheless, the increase in contrast observed in the ΔR_1 and Δf (see Fig. 5), when taking into account the phantom study results (Fig. 1), suggest Mn^{2+} enrichments are of the same order of magnitude, further supporting a close association between R_1, frequency shift increase and Mn^{2+} uptake. For the maximum Mn^{2+} dosage (125 mg/Kg), assuming relaxivity values hold in vivo, the following enrichments can be calculated: 21 μM in the Cortex, 63 μM in the DG, and 37 μM in the OB.

The evaluation of the CNR increase following Mn^{2+} administration indicated that, overall, from 0 to 125 mg/kg, Mn^{2+} enhancement was more pronounced in phase imaging than in T_1-weighted imaging protocol used although its fractional increase was greater for the latter (see Table 1). This observation is highly dependent on the sequence and parameters used to obtain the T_1-weighted images. In this study, a gradient echo with a fixed TR of 1 second was applied to avoid respiration induced artifacts, under such constraints the optimal flip angle to obtain T_1 contrast is ~90°. Had our setup allowed for a three-dimensional acquisition, a TR as short as 10 ms could have been used together with an excitation of 11° which would have increased our contrast per unit of time to the ΔR_1 by ~10%. Other studies in literature have used spin echo sequences (9,10) or inversion recovery sequences (4). The use of a gradient echo with a short echo time was preferred to a spin echo sequence due to the B_1 inhomogeneity associated with the use of a surface coil. The signal from a spin echo sequence has a $\sin^3(90^*B_1)$ dependence on B_1 (33), significantly limiting the range over which acceptable SNR

and T_1-weighting would be achieved on our setup and which can only be overcome by the usage of adiabatic refocusing pulses (34). A gradient echo sequence introduces a Mn^{2+} related signal attenuation due to T_2* decay. The reduction in contrast due to the use of a gradient echo sequence (given an apparent transverse relaxivity of Mn^{2+}) is bound to be smaller than 50% for the largest Mn^{2+} dose, not enough to justify the 4–7 times reduction in T_1-weighted contrast in respect to phase found in Table 1. Although it has been demonstrated inversion recovery-based sequences (such as the MPRAGE) offer superior T_1-contrast with reduced sensitivity to B_1 homogeneity thanks to the use of adiabatic inversion pulses and efficient low flip angle excitations for the readout, analytical analysis of the contrast efficiency (35) of the spoiled gradient echo used in this study versus an MPRAGE sequence with the same echo time, constraint of 128 phase encoding steps per excitation (TR = 2–4 s, flip angle = 8 TI = 1.5 s) showed that the MPRAGE would not necessarily provide an improved T_1-weighted contrast in comparison to our protocol when considering the typical relaxation parameters measured in the dentate gyrus (R_1 of 0.46 s^{-1} and a ΔR_1 of 0.35s^{-1} following Mn^{2+} systemic administration at maximum dose of 125 mg/kg). It is important to point out that, as the magnetic susceptibility induced frequency shift is linearly dependent to the static magnetic field, at lower magnetic fields (such as the typically available for animal scanning 4.7–7T), the CNR of the phase contrast will be lower and it remains to be determined at which field strength an optimized T_1-weighted imaging protocol is likely to outperform phase imaging.

One of the pitfalls of in vivo phase imaging is its sensitivity to physiology and respiration induced artifacts due to the long echo time used. In our study, such artifacts were minimized by using respiration triggering. Another important limitation of phase imaging is the difficulty of obtaining reliable values in regions close to air/tissues interfaces such as the olfactory bulb. Despite the care taken when performing background filtering, the phase image in the olfactory bulb is pronouncedly affected by phase variations arising from air/tissue interfaces making structures situated at the extremities (such as the olfactory glomeruli, the glomerular layer) difficult to discern.

Phase-based MEMRI can, potentially, offer a higher resolution and contrast than that obtainable with T_1-weighted imaging and be equally quantitative. To make phase-based Mn^{2+} quantification, it would be important to perform a quantitative susceptibility mapping (36,37). The lack of this step on our analysis is likely to explain the difference in ordering observed between the frequency shift enhancement in the olfactory bulb, hippocampus, and in R_1 maps. The measured frequency shift reflects not only the local increase of the Mn^{2+} uptake, but also its geometrical shape in respect to the static magnetic field. To be able to compute susceptibility maps, it would be beneficial to obtain a closer to isotropic resolution and bigger coverage than what was achievable with a surface coil. Two of the main difficulties when evaluating susceptibility maps is the fact that the forward model (role of macromolecular contribution (15), anisotropic susceptibility (38), and microstructure (14)) is not fully understood and that the susceptibility values should be always seen as relative measure. In the case of studying Mn^{2+} uptake, Mn^{2+} can be considered as simple isotropic susceptibility contrast agent while any other bias of the QSM method will be the same prior and post to Mn^{2+} infusion. Also, from the results observed in this study using R_1 mapping (see Fig. 5a), white matter structures would form an ideal reference throughout the enrichment. Such an approach would offer fully quantitative Mn^{2+} uptake maps.

CONCLUSIONS

We conclude from the present study that MEMRI can be assessed by phase imaging at high magnetic field. Although Mn^{2+} had a stronger effect on T_1-weighted imaging, phase imaging demonstrated to have superior CNR following Mn^{2+} systemic administration. Future work will be directed toward exploring high resolution and high contrast manganese enhanced phase images to obtain quantitative manganese uptake information by using quantitative susceptibility mapping.

ACKNOWLEDGMENTS

We thank Dr. Arthur Magill for the assistance given to the RF hardware. Supported in part by the EPFL-Merck Serono alliance, this study was supported by the Centre d'imagerie biomédicale of the UNIL, EPFL, UNIGE, CHUV and HUG as well as the Jeantet and Leenaards foundations.

APPENDIX 1

For a given echo time and as [Mn^{2+}] increases, the increased magnetic susceptibility induces an increase in phase but also a reduction in gradient echo (GRE) signal intensity due to T_2* attenuation. As phase CNR is correlated to both magnitude SNR and phase difference for a given echo time, MEMRI assessment by phase imaging at ultra-high field could be hampered by high [Mn^{2+}] if the reduction in T_2* is large, relative to the echo time used. To address this point, simulations were performed using a range of Mn^{2+} concentrations going beyond those found in the in vivo rodent brain following Mn^{2+} systemic administration (30). The GRE signal was simulated using the relaxation parameters experimentally found for the Dentate Gyrus ($R_{1control}$, ΔR_1 at maximum dose of 125 mg/kg) and Mn^{2+} relaxivities (reported in Section *Relaxivity r_1* and δf_{pmM} of *Mn^{2+} at 14.1T*). The GRE magnitude CNR was defined as the signal difference prior and post Mn^{2+} infusion (125 mg/kg). Phase CNR was defined similarly and as described in Eq. [3].

Figure A1 (a, b) shows the expected magnitude CNR for a 90 degree and Ernst angle setting respectively. As expected, in both cases the maximum GRE CNR is at TE = 0. However, due to the T_2* decay, a very fast CNR decrease is observed for the Ernst angle setting resulting in a decrease of magnitude signal as the echo time increases for high Mn^{2+} concentration. However, this decrease in signal intensity does not suggest a reduction of the phase CNR as it can be observed in Figure A1c.

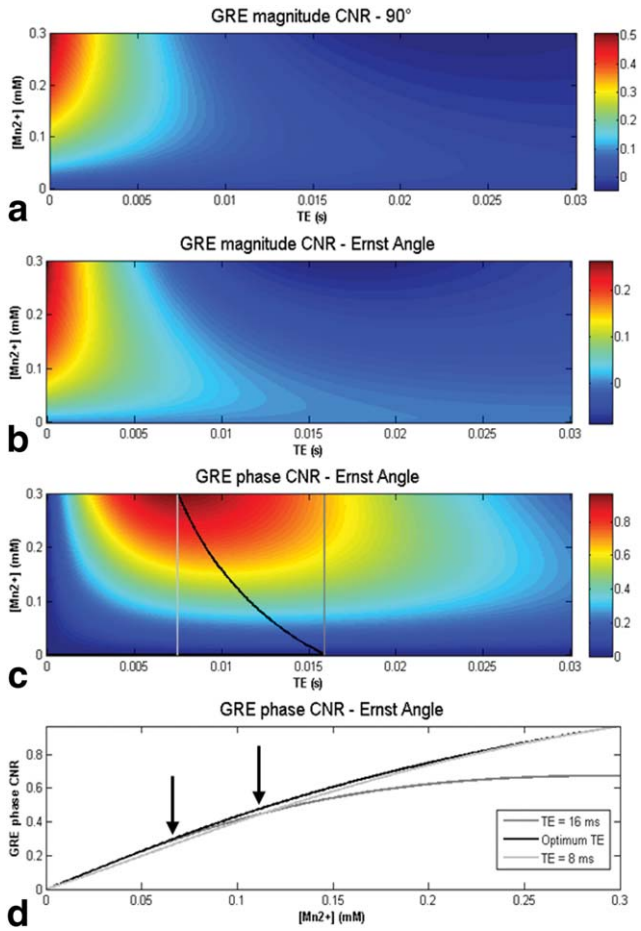

FIG. A1. **a,b:** Magnitude and (**c**) phase contrast to noise ratio of the GRE signal associated with the dentate gyrus as function of the Mn^{2+} concentration and echo time at 90° (a) and at the Ernst angle (b–d). In Figure A1.c, the black line shows the optimum echo time for a given Mn^{2+} concentration. The dark and light gray lines show the optimum echo time respectively at control and post Mn^{2+} infusion for the highest concentration. The plot in (**d**) shows the evolution of the phase CNR for these three different echo times. Black arrows point to the maximum Mn^{2+} concentration obtained in our study (0.064 mM for the Dentate Gyrus) and reported in literature [0.11 mM in Olfactory Bulb (30)].

Nevertheless it suggests that the optimum echo time should be reduced for higher Mn^{2+} concentrations (as shown by the black line). The optimum echo time decreases from 16 ms to 8 ms (at $[Mn^{2+}] = 0.3$ mM) due to the T_2* decay. The plot in Figure A1d shows that, if the optimum echo at pre-Mn^{2+} infusion is indeed kept constant, the phase CNR starts to saturate at high concentrations of Mn^{2+} (as shown by the dark gray line) although the frequency difference would continue to increase linearly.

Consequently, the use of a shorter echo time for post Mn^{2+} enrichment would have been preferable as it can be observed at TE = 8 ms where the phase CNR evolution is close to optimum (light gray line). However, when taking into account the range of Mn^{2+} concentration obtained in the study (0 to 0.064 mM), at TE = 16 ms no saturation effect is observed as the phase CNR increased linearly with the increased tissue $[Mn^{2+}]$.

REFERENCES

1. Chandra SV, Shukla GS. Role of iron deficiency in inducing susceptibility to manganese toxicity. Arch Toxicol 1976;35:319–323.
2. Wolf GL, Baum L. Cardiovascular toxicity and tissue proton T1 response to manganese injection in the dog and rabbit. AJR Am J Roentgenol 1983;141:193–197.
3. Jankovic J. Searching for a relationship between manganese and welding and Parkinson's disease. Neurology 2005;64:2021–2028.
4. Tucciarone J, Chuang KH, Dodd SJ, Silva A, Pelled G, Koretsky AP. Layer specific tracing of corticocortical and thalamocortical connectivity in the rodent using manganese enhanced MRI. Neuroimage 2009;44:923–931.
5. Yu X, Wadghiri YZ, Sanes DH, Turnbull DH. In vivo auditory brain mapping in mice with Mn-enhanced MRI. Nat Neurosci 2005;8:961–968.
6. Aoki I, Wu YJ, Silva AC, Lynch RM, Koretsky AP. In vivo detection of neuroarchitecture in the rodent brain using manganese-enhanced MRI. Neuroimage 2004;22:1046–1059.
7. Silva AC, Lee JH, Wu CW, Tucciarone J, Pelled G, Aoki I, Koretsky AP. Detection of cortical laminar architecture using manganese-enhanced MRI. J Neurosci Methods 2008;167:246–257.
8. Morita H, Ogino T, Seo Y, Fujiki N, Tanaka K, Takamata A, Nakamura S, Murakami M. Detection of hypothalamic activation by manganese ion contrasted T(1)-weighted magnetic resonance imaging in rats. Neurosci Lett 2002;326:101–104.
9. Lee JH, Silva AC, Merkle H, Koretsky AP. Manganese-enhanced magnetic resonance imaging of mouse brain after systemic administration of MnCl2: dose-dependent and temporal evolution of T1 contrast. Magn Reson Med 2005;53:640–648.
10. Chuang KH, Belluscio L, Koretsky AP. In vivo detection of individual glomeruli in the rodent olfactory bulb using manganese enhanced MRI. Neuroimage 2010;49:1350–1356.
11. Duyn JH, van Gelderen P, Li TQ, de Zwart JA, Koretsky AP, Fukunaga M. High-field MRI of brain cortical substructure based on signal phase. Proc Natl Acad Sci U S A 2007;104:11796–11801.
12. Rauscher A, Sedlacik J, Barth M, Mentzel HJ, Reichenbach JR. Magnetic susceptibility-weighted MR phase imaging of the human brain. AJNR Am J Neuroradiol 2005;26:736–742.
13. Marques JP, Maddage R, Mlynarik V, Gruetter R. On the origin of the MR image phase contrast: an in vivo MR microscopy study of the rat brain at 14.1 T. Neuroimage 2009;46:345–352.
14. He X, Yablonskiy DA. Biophysical mechanisms of phase contrast in gradient echo MRI. Proc Natl Acad Sci U S A 2009;106:13558–13563.
15. Zhong K, Leupold J, von Elverfeldt D, Speck O. The molecular basis for gray and white matter contrast in phase imaging. Neuroimage 2008;40:1561–1566.
16. Fukunaga M, Li TQ, van Gelderen P, et al. Layer-specific variation of iron content in cerebral cortex as a source of MRI contrast. Proc Natl Acad Sci U S A 2010;107:3834–3839.
17. Schweser F, Deistung A, Lehr BW, Reichenbach JR. Quantitative imaging of intrinsic magnetic tissue properties using MRI signal phase: an approach to in vivo brain iron metabolism? Neuroimage 2011;54:2789–2807.
18. Lodygensky GA, Marques JP, Maddage R, Perroud E, Sizonenko SV, Huppi PS, Gruetter R. In vivo assessment of myelination by phase imaging at high magnetic field. Neuroimage 2012;59:1979–1987.
19. Liu C, Li W, Johnson GA, Wu B. High-field (9.4 T) MRI of brain dysmyelination by quantitative mapping of magnetic susceptibility. Neuroimage 2011;56:930–938.
20. Lee J, Shmueli K, Kang BT, Yao B, Fukunaga M, van Gelderen P, Palumbo S, Bosetti F, Silva AC, Duyn JH. The contribution of myelin to magnetic susceptibility-weighted contrasts in high-field MRI of the brain. Neuroimage 2012;59:3967–3975.
21. Gruetter R. Automatic, localized in vivo adjustment of all first- and second-order shim coils. Magn Reson Med 1993;29:804–811.
22. Gowland P, Mansfield P. Accurate measurement of T1 in vivo in less than 3 seconds using echo-planar imaging. Magn Reson Med 1993;30:351–354.
23. Chuang KH, Koretsky A. Improved neuronal tract tracing using manganese enhanced magnetic resonance imaging with fast T(1) mapping. Magn Reson Med 2006;55:604–611.
24. van der Zwaag W, Marques JP, Lei H, Just N, Kober T, Gruetter R. Minimization of Nyquist ghosting for echo-planar imaging at ultra-

high fields based on a "negative readout gradient" strategy. J Magn Reson Imaging 2009;30:1171–1178.
25. Nelder JA, Mead R. A Simplex-Method for Function Minimization. Comput J 1965;7:308–313.
26. Goldstein RM, Zebker HA, Werner CL. Satellite radar interferometry - two-dimensional phase unwrapping. Radio Sci 1988;23:713–720.
27. Marques JP, Bowtell RW. Using forward calculations of the magnetic field perturbation due to a realistic vascular model to explore the BOLD effect. NMR Biomed 2008;21:553–565.
28. Kukley M, Capetillo-Zarate E, Dietrich D. Vesicular glutamate release from axons in white matter. Nat Neurosci 2007;10:311–320.
29. Silva AC, Lee JH, Aoki I, Koretsky AP. Manganese-enhanced magnetic resonance imaging (MEMRI): methodological and practical considerations. NMR Biomed 2004;17:532–543.
30. Chuang KH, Koretsky AP, Sotak CH. Temporal changes in the T1 and T2 relaxation rates (DeltaR1 and DeltaR2) in the rat brain are consistent with the tissue-clearance rates of elemental manganese. Magn Reson Med 2009;61:1528–1532.
31. Lee J, Hirano Y, Fukunaga M, Silva AC, Duyn JH. On the contribution of deoxy-hemoglobin to MRI gray-white matter phase contrast at high field. Neuroimage 2010;49:193–198.
32. Kelly KM, Ikonomovic MD, Abrahamson EE, Kharlamov EA, Hentosz TM, Armstrong DM. Alterations in hippocampal voltage-gated calcium channel alpha 1 subunit expression patterns after kainate-induced status epilepticus in aging rats. Epilepsy Res 2003;57:15–32.
33. Haacke EM. Magnetic resonance imaging: physical principles and sequence design. New York: Wiley; 1999. xxvii, 914 p.
34. van de Looij Y, Kunz N, Huppi P, Gruetter R, Sizonenko S. Diffusion tensor echo planar imaging using surface coil transceiver with a semiadiabatic RF pulse sequence at 14.1T. Magn Reson Med 2011;65:732–737.
35. Marques JP, Kober T, Krueger G, van der Zwaag W, Van de Moortele PF, Gruetter R. MP2RAGE, a self bias-field corrected sequence for improved segmentation and T1-mapping at high field. Neuroimage 2010;49:1271–1281.
36. Wharton S, Bowtell R. Whole-brain susceptibility mapping at high field: a comparison of multiple- and single-orientation methods. Neuroimage 2010;53:515–525.
37. Shmueli K, de Zwart JA, van Gelderen P, Li TQ, Dodd SJ, Duyn JH. Magnetic susceptibility mapping of brain tissue in vivo using MRI phase data. Magn Reson Med 2009;62:1510–1522.
38. Liu C. Susceptibility tensor imaging. Magn Reson Med 2010;63:1471–1477.